Fiber-type optomechanical array using high-Q microbottle resonators

Motoki Asano,* Hiroshi Yamaguchi, and Hajime Okamoto
NTT Basic Research Laboratories, NTT Corporation, 3-1 Morinosato Wakamiya, Atsugi-shi, Kanagawa 243-0198, Japan

(Received 16 October 2023; revised 27 December 2023; accepted 5 January 2024; published 7 February 2024)

We demonstrate a fiber-type optomechanical array consisting of elastically interconnected silica microbottle resonators with high-Q optical and mechanical modes. In total, 50 optomechanical resonators fabricated by fine glass processing are uniformly arrayed on a silica fiber. Evanescent coupling of a tapered optical fiber to an arbitrary resonator allows for highly sensitive readout and efficient actuation of mechanical motion at an arbitrary position in the array. Phonon propagation through the 50 microbottles is achieved by both linearly and parametrically driving a mechanical mode at one end and by detecting it at the other end. This optomechanical array is scalable, tunable, and lithography-free and can be extended to fiber-based sensory applications with structural flexibility and operability in various environments.

DOI: 10.1103/PhysRevApplied.21.024013

I. INTRODUCTION

Cavity optomechanics offers highly sensitive readout and efficient driving of mechanical motion via an optomechanical coupling between cavity photons and phonons [1]. Multiple cavity optomechanical devices that have optical and or elastic couplings have recently been developed [2–5]. Such a cavity optomechanical array has three distinct advantages: scalable expansion of the number of photonic and phononic modes; interconnection between the spatially distant resonator nodes with energy transfer; and appearance and control of nontrivial many-body effects (e.g., nonreciprocal transmission). The arrays are applicable to multimode optomechanical sensors, information routing of photons and phonons, and fundamental studies based on analogies to many-body systems, such as PT symmetry [6–8], Anderson localization [9–11], artificial gauge [12,13], and topological propagation [14,15].

Cavity optomechanical arrays have so far been demonstrated using on-chip optomechanical resonators, such as photonic-phononic crystal cavities [14,15] and whispering gallery mode (WGM) optomechanical resonators [16]. Sophisticated semiconductor fabrication techniques have been used to make photonic-phononic crystal cavities through optical and elastic couplings. Arrays of on-chip WGM optomechanical resonators, such as microdisks, have been built by utilizing strong photon-photon couplings via the optical evanescent field. Various demonstrations have been reported, such as on phononic topological propagation [14,15] and mechanical synchronization [16], but the fixed-by-design on-chip architecture cannot be extended to on-demand applications, such as externally tunable devices [17,18] and free-access sensors [19,20].

In this paper we focus on another candidate, namely, fiber-type optomechanical resonators, such as microspheres and microbottles. Fiber-type systems have the following outstanding properties that on-chip devices do not have: lithography-free formability, structure flexibility, and operability in various environments, while maintaining their excellent intrinsic optomechanical performance [21,22]. Coupled array structures are expected to enable novel functions in fiber-based technology.

Here, we built a fiber cavity optomechanical array, referred to as a chained-microbottle resonator (CMBR), consisting of elastically coupled microbottle resonators. The CMBR includes 50 microbottle resonators in total and is fabricated through fine glass processing. Each microbottle has an optomechanical coupling between high-Q optical WGMs and high-Q mechanical radial-breathing modes (RBMs) via radiation pressure and can be used for highly sensitive readout and efficient actuation of mechanical motion [see Fig. 1(a)]. The optomechanical coupling in the CMBR is selectively activated at an arbitrary node by injecting laser light into individual WGMs by utilizing a tapered optical fiber. While the optical WGMs are locally confined in each microbottle, the mechanical RBMs are coupled with the adjacent nodes because of their spatial modes overlap in the fiber axial directions. Thus, owing to the mechanical couplings, optically driven mechanical motion at a resonator is transferable along the one-dimensional array and can be sensitively detected at the arbitrary resonator through the optomechanical coupling. When the mechanical couplings among all of the nodes are in the strong coupling regime, phonon

*motoki.asano@ntt.com

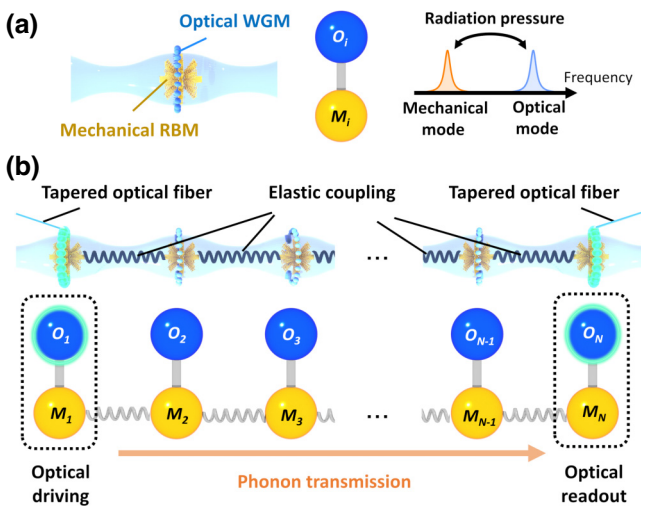

FIG. 1. (a) Schematic diagram of a microbottle resonator, which is an element of the CMBR, with an optomechanical coupling between the optical WGM and mechanical RBM. (b) Schematic diagram of the CMBR including optomechanical and elastic coupling. Laser light (colored green) is guided into an arbitrary microbottle by using a tapered optical fiber. By combining optical driving and readout of the mechanical mode (e.g., at the first and Nth nodes, respectively), phonon propagation over the CMBR is possible.

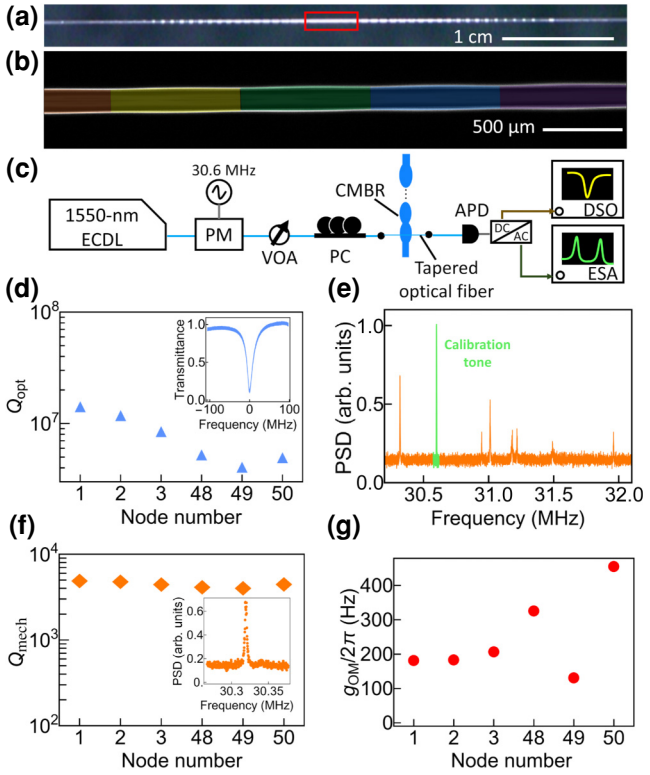

FIG. 2. (a) Optical microscope image of the whole structure of the CMBR. (b) Optical microscope image with a focused view of the CMBR around the area outlined in red in (a). Each microbottle is shaded in different colors. (c) Schematic diagram of the experimental setup for evaluating optical properties and observing the thermal fluctuation of the mechanical modes in each microbottle. The abbreviations are as follows: variable optical attenuator, VOA; polarization controller, PC; avalanche photodiode, APD; optical phase modulator, PM; digital sampling oscilloscope, DSO; electric spectrum analyzer, ESA. (d) Optical Q factors obtained in the first, second, third, 48th, 49th, and 50th microbottles. The inset shows a typical transmission spectrum obtained in the first microbottle. (e) Power spectral density (PSD) of the thermal fluctuation of the mechanical modes and the calibration tone (at 30.6 MHz) in the first microbottle. The calibration tone for estimating g_{OM} is colored green. (f) Mechanical Q factors obtained in the six microbottles. (g) Vacuum optomechanical coupling constants obtained in the six microbottles.

propagation between the two resonators at the ends becomes possible [see Fig. 1(b)]

II. EXPERIMENT

A. Device

The CMBR was fabricated on a silica optical fiber and included 50 microbottle nodes ($N = 50$) made by periodically forming 51 bottlenecks via the heat-and-pull technique [23]. To maintain the uniformity of the microbottle structures, the tension between the ends of the silica fiber was monitored before pulling to form each neck. Figure 2(a) shows an optical microscope image of the whole structure and Fig. 2(b) shows an enlargement including five microbottle structures. Each node consists of a 125-μm-diameter bottle with about 115-μm-diameter necks and neck-to-neck length of about 700 μm (i.e., the whole device length is about 3.5 cm).

The optical resonance of the CMBR was observed by using the probe setup shown in Fig. 2(c). An external cavity diode laser (ECDL) operating at wavelengths around 1550 nm was used for probing the optical transmission spectrum by scanning its frequency with appropriate optical power (around 1 mW) and polarization. All measurements were made under atmospheric conditions. The optical transmission spectra in six microbottles (the first, second, third, 48th, 49th, and 50th) were measured by adjusting the contact position of the tapered optical fiber with the CMBR. Figure 2(d) shows typical optical Q factors in each microbottle. The average optical Q factors among the six resonators reached $\bar{Q}_{\mathrm{opt}} = 8.3 \times 10^6$, which is comparable to a standard WGM resonator.

These high-Q optical resonances provide high displacement sensitivity, and they allowed us to probe the thermal fluctuations of the mechanical RBMs. Note that the probe laser frequency was thermally locked in the middle of the slope of cavity resonances [24]. The power spectral density at the 50th node is shown in Fig. 2(e). The power spectra of the thermal fluctuations can be utilized for estimating

the mechanical Q factors and the vacuum optomechanical coupling constants, defined as $g_{\mathrm{OM},j} \equiv x_{\mathrm{zpf},j}\,\partial\omega_{\mathrm{opt},j}(x)/\partial x$ where $\omega_{\mathrm{opt},j}$ is the optical frequency as a function of the mechanical displacement x, and $x_{\mathrm{zpf},j}$ is the zero-point fluctuation of the mechanical mode in the jth microbottle ($j = 1, 2, 3, 48, 49, 50$). Here, they were evaluated in the lowest frequency mode as a representative example. The mechanical Q factors were over 10^3, and their average value reached $\bar{Q}_{\mathrm{mech}} = 4.8 \times 10^3$, which is comparable to standard WGM optomechanical resonators [see Fig. 2(f)]. The vacuum optomechanical coupling constant was quantified by comparing the thermal fluctuation and the calibration tone from an optical phase modulator (PM) [25]. The average vacuum optomechanical coupling constant among the six resonators reached $\bar{g}_{\mathrm{OM}}/2\pi = 246$ Hz [see Fig. 2(g)]. The single optomechanical node thus acted like a high-Q optomechanical resonator in the same way as the previously reported single- [21,22] and twin-microbottle structures [19,20].

Multiple thermal fluctuation peaks appeared in the PSD, and they originated from two different sources. One source is the multiple axial modes in the microbottle structure, whose frequency separations are several hundred kilohertz. The other is the elastic couplings among the adjacent nodes, whose frequency separations are several tens of kilohertz. The frequency separation corresponds to the elastic coupling strength, which is larger than the mechanical linewidth. For instance, the double peaks around 31 MHz in Fig. 2(e) reflect the elastic coupling strength $g_M/2\pi = 42.8$ kHz, which is about ten times larger than the mechanical dissipation.

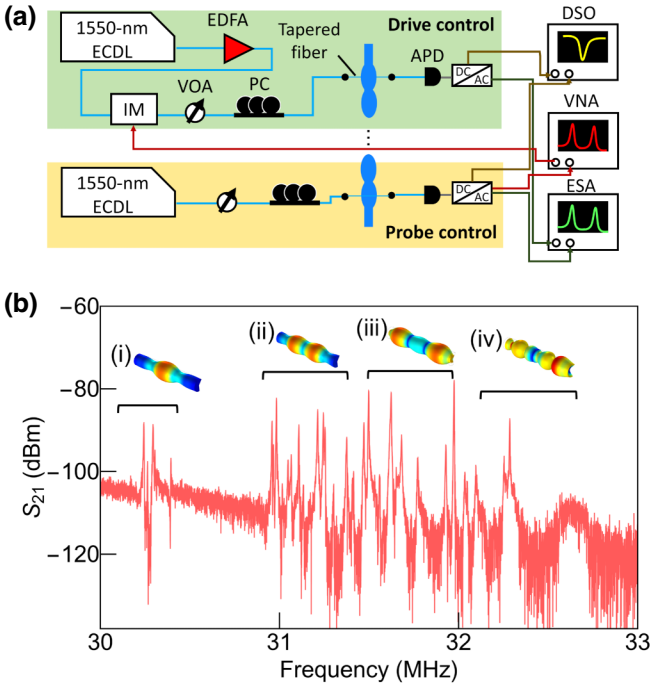

FIG. 3. (a) Schematic diagram of the experimental setup for phonon propagation in the CMBR. The abbreviations are the same as in Fig. 2, with additional ones as follows: erbium-doped fiber amplifier, EDFA; intensity modulator, IM; vector network analyzer, VNA. (b) A phonon transmission spectrum in the CMBR while optomechanical driving and detection are performed at both ends. The insets show the spatial profile of the radial breathing modes with the (i) first-, (ii) second-, (iii) third-, and (iv) fourth-order axial mode numbers calculated in the finite-element-method simulation (see Appendix A).

B. Phonon transmission spectrum

Owing to the existence of elastic couplings between the adjacent nodes, the mechanical vibration driven via optomechanical coupling is guided over the CMBR between the ends. Here, we contacted the tapered optical fiber on the first and 50th nodes for optical driving and detection of mechanical vibration, respectively. The phonon transmission spectrum was obtained by driving the mechanical vibration at the first node by using intensity-modulated light from an intensity modulator (IM) and by detecting the propagated vibrations at the 50th node by using a probe laser [see Fig. 3(a)]. The power of the drive and probe laser was set to about 10 mW and 1 mW, respectively. Figure 3(b) shows the phonon transmission spectra (S_{21} signal) monitored with a vector network analyzer (VNA) in which the rf drive port was connected to the IM for the drive laser and the detection port was connected to the photodiode for the probe laser. Whereas the thermal fluctuation measurement reflected the local projection of the coupled mechanical modes, this driven measurement unveils the transfer function in the CMBR. Thus, the multiple peaks in the spectra are evidence of the elastic interconnection between the two ends.

To clarify the contribution from the higher-order axial modes, we performed a finite-element-method (FEM) simulation by using COMSOL MULTIPHYSICS (see Appendix A). The insets in Fig. 3(b) show the displacement profile of each axial mode calculated with periodic boundary conditions. Because the higher-order axial modes have large mode overlaps between the adjacent nodes, the mechanical couplings in those modes (31–32 MHz) become stronger than those in the lower-order axial modes (around 30.2 MHz). This caused the transmitted amplitude in the higher-order axial modes to be larger than those in the lower-order ones. Moreover, many spectra show positive skewness; that is, the spectra are biased to the negative frequency. This positive skewness can be partly understood as the modified stress condition where the stress around the center area is concentrated due to the deflection of the CMBR (see Appendix B). The CMBR thus operated as a phonon waveguide in which the vibrating energy is transferred between the two ends.

C. Parametric oscillation and its propagation

High-Q optomechanical resonators provide optomechanical parametric oscillations whereby the extremely narrow linewidths in the self-oscillation phonon states can be used in sensor applications [26–28]. Since the oscillation threshold is proportional to $Q_{\mathrm{opt}}^{-2}Q_{\mathrm{mech}}^{-1}$ [29], the high-Q CMBR can efficiently induce parametric oscillation and transmit self-oscillating phonon states through elastic coupling. The optomechanical coupling in each microbottle provides an optomechanical gain, Γ_{OM}, by using a blue-detuned laser whose detuning is close to the sum of the optical and mechanical resonance frequencies. When the optomechanical gain is larger than the total dissipation, a mechanical mode starts to oscillate. Because the optomechanical coupling is localized in each resonator, the parametric optomechanical oscillation occurs in a mechanical mode in the single microbottle in contact with the tapered optical fiber. This local parametric oscillation becomes more dominant as the number of nodes increases (see Appendix C).

Owing to such a local parametric oscillation, the oscillating phonon at the first node propagates to the 50th node via mechanical coupling [Fig. 4(a)]. Here, the threshold of the local parametric oscillation was evaluated by setting the laser frequency in the blue-detuned regime for both oscillating and probing the mechanical mode at the first node. The threshold optical power of 12.2 mW was determined from the input optical power dependence [Fig. 4(b)]. The oscillation amplitude in Fig. 4(b) was estimated through a fast Fourier transformation while scanning the laser frequency. Propagation of the mechanical oscillation was demonstrated by using two tapered optical fibers for pumping and probing at the first and the 50th node, respectively. Figures 4(c) and 4(d) show the radio-frequency power spectra observed in the first and the 50th node, respectively, with an optical pump power of $P_D = 20.3$ mW [the optical power at the probe node is ten times smaller than the drive (about 200 μW)]. The mechanical oscillation signal was observed in the first and the 50th nodes, which is evidence of phonon propagation of the local parametric oscillation signal. The degradation of the signal-to-noise ratio between the first node (about 90 dB) and the 50th node (about 40 dB) originates from phonon loss in the phonon propagation direction and coupling loss due to the mechanical frequency deviation. In addition to the signal in the frequency domain, the oscillating periodic signals in the time domain at the first and 50th nodes reflected the conservation of signal coherence through the phonon propagation [see Figs. 4(e) and 4(f)].

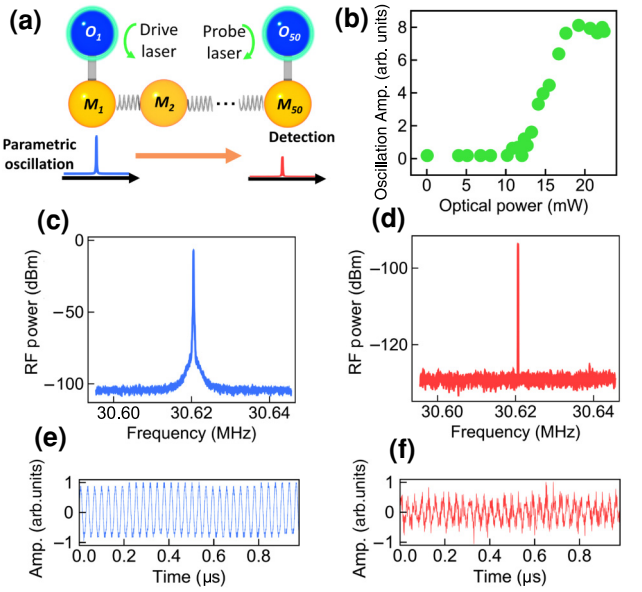

FIG. 4. (a) Schematic diagram of phonon propagation with parametric optomechanical oscillation. (b) Mechanical oscillation amplitude with respect to the input optical power at the first node. The parametric oscillation occurs at a threshold optical power of 12.2 mW. (c), (d) Radio-frequency power spectra of optomechanical parametric oscillation observed at the first node (c) and 50th node (d). (e),(f) Time-domain signals of optomechanical parametric oscillation observed at the first node (e) and 50th node (f).

III. DISCUSSION

The CMBR was fabricated by forming a microbottle structure one-by-one, which is a completely different fabrication process from that of on-chip coupled mechanical resonators (e.g., the wet etching process). The geometry of each element is tunable by sequentially fabricating and evaluating each microbottle [30]. This adaptive fabrication process will not only decrease the deviations in the mechanical properties of microbottles such as the resonance frequency and linewidth, but also introduce more functional phononic structures, such as point defects [31] and zero-dimensional topological edges [32–34].

The simple and selective laser input by using tapered optical fibers allows us to increase the number of control cavity nodes. Although this proof-of-principle experiment was done by simultaneously injecting the laser light into two microbottle resonators, utilizing more laser inputs by using multiple tapered optical fibers can be done to perform more sophisticated phonon routing by combining optomechanical cooling, amplification, and nonlinearity [35–38]. In particular, optomechanical cooling, such as feedback cooling and resolved-sideband cooling, of the coupled multiple resonators has the potential to locally decrease the number of thermal occupations of the coupled mechanical modes. This will provide a platform to explore nonequilibrium physics in phononic thermal flow [39,40] and quantum ground state cooling [5,41,42].

The fiber-type geometry of the cavity optomechanical array enables us to readily use the device in liquid environments [43–45], similarly to our previously reported

twin-microbottle resonator [19,20]. The CMBR can extend the optomechanical sensing in the liquid with respect to the dynamic range and the spatial resolution. By setting the first node in air and the other nodes in the liquid, the applicable immersion depth increases with the number of microbottles in the liquid. This deep depth capability enables the vertical structural properties of liquids, such as liquid-liquid interfaces, to be explored. Moreover, local stimulation (e.g., particle adhesion) on a microbottle in the CMBR causes a change in the spectral shape of the hybridized mechanical mode [46]. It can be used to spatially resolve the local stimulation along the CMBR in the liquid. Furthermore, the structural flexibility of the silica fibers makes it possible to use a unique configuration in which the microbottles in the central region are partially immersed in the liquid through the deflection of the fibers while holding the other microbottles in air. This configuration will open the way to more advanced optomechanical sensings, for example, time-resolved measurement and particle detection based on the Anderson localization [47,48] via phonon propagation.

IV. CONCLUSION

We demonstrated a fiber-type optomechanical array using a chained-microbottle resonator. The array consisted of 50 high-Q microbottle resonators that were elastically interconnected through fine glass processing. Phonon propagation over the CMBR was demonstrated by combining optical linear (and parametric) driving at one end of the array and sensitive detection of mechanical motion at the other end. The high scalability, accessibility of each resonator, and controllability with a high-Q optical cavity will expand the applications of optomechanical arrays with unique fiber properties, such as structural flexibility and operability in various environments.

ACKNOWLEDGMENTS

This work was supported by JSPS KAKENHI (21H01023, 23H05463).

APPENDIX A: FINITE-ELEMENT-METHOD SIMULATIONS

To examine the mechanical axial mode distributions, we calculated the mechanical eigenmodes in our CMBR structure by utilizing a finite-element-method (FEM) simulator (COMSOL MULTIPHYSICS). Here, periodic boundary conditions were imposed on a microbottle structure (maximum diameter of 125 μm, neck diameter of 115 μm, and neck separation length of 700 μm) so as to achieve the mechanical band structure. As shown in Fig. 5 different modes with respect to the axial mode number appear in each mechanical band. In contrast to the higher-order axial modes, the lower-order axial modes are strongly confined

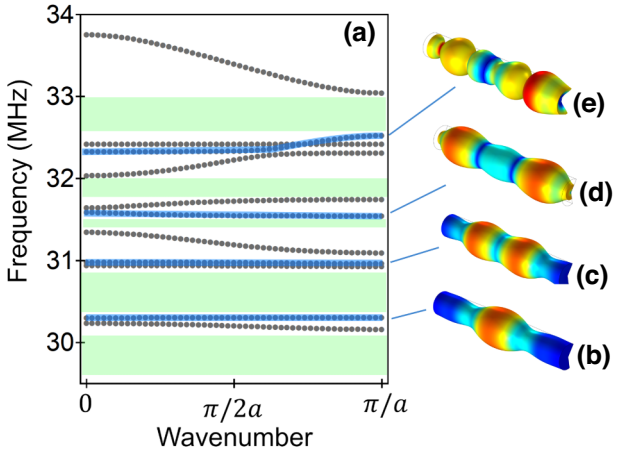

FIG. 5. (a) The mechanical band structure for different axial-order RBMs colored blue. The green shaded areas correspond to the band gap. (b)–(e) Spatial distributions of the first- (b), second (c), third (d), and fourth order (e) of the axial number.

around the center of the microbottle structure. This implies that the lower-order axial modes have a smaller elastic coupling than the higher ones do because of the small internode mode overlap, which causes the local parametric oscillation discussed in the main text.

APPENDIX B: EFFECT OF THE MODIFIED STRESS CONDITION

The modified stress condition was investigated by shifting the mechanical frequency in the microbottle located

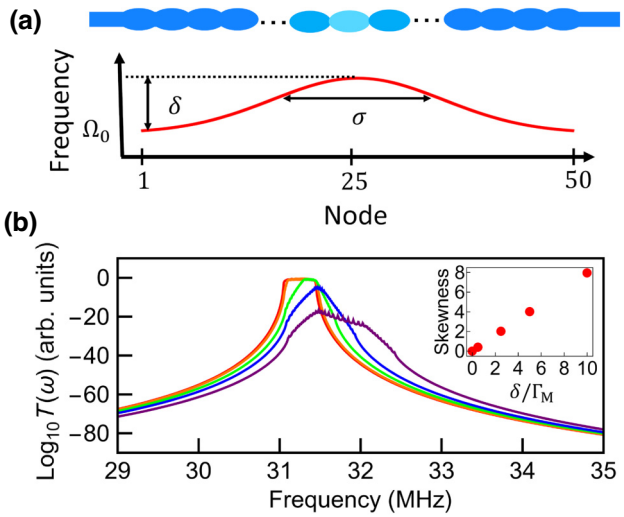

FIG. 6. (a) Schematic diagram of the modified stress condition along the CMBR. (b) Calculated transmission spectra $T(\omega)$ with respect to different modulation depths (red, $\delta = 0$; orange, $\delta = 0.5\Gamma_M$; green, $\delta = 2.5\Gamma_M$; blue, $\delta = 5\Gamma_M$; purple, $\delta = 10\Gamma_M$). The inset shows the corresponding skewness which apparently increases with increasing modulation depth.

in the center area of the CMBR. The mechanical frequency distribution with respect to the node is modeled by $\Omega_j = \Omega_0 + \delta \exp\left[-(j - N/2)^2/(2\sigma^2)\right]$ with the modulation depth, δ, and the modulation width, $\sigma > 0$ [see Fig. 6(a)]. The transmission spectrum, $T(\omega)$, is given by

$$T(\omega) = |[\mathbf{Mf}]_N|^2$$

where $\mathbf{M}$ represents the mechanical susceptibility matrix, $\mathbf{f} = (1, 0, 0, \ldots, 0)^T$ corresponds to the driving force localized in the first microbottle, and $[\mathbf{a}]_N$ denotes the Nth element in the vector $\mathbf{a}$. By setting $N = 50$ and $\sigma = N/4$, the modulation depth dependence was investigated by changing δ in the positive region. As shown in Fig. 6(b), the transmittance and 3-dB bandwidth decrease with increasing δ because the distortion in uniformity causes a net decoupling among the mechanical resonators. Moreover, this frequency modulation results in the skewness of the transmission spectra. A positive frequency shift induces a positive skewness. Because this positive skewness appears in the phonon transmission spectra in the experiment [see Fig. 3(b)], it is considered that the stress concentrated in the central region of the CMBR due to the fiber deflection changes the phonon transmission. Note that we confirmed that $\delta < 0$ reflects the negative skewness.

APPENDIX C: LOCAL PARAMETRIC OSCILLATION

Here, we consider local parametric oscillation at the first node (i.e., an edge node in the CMBR) where the other coupled $N - 1$ mechanical nodes act as a dissipation channel. To simplify the discussion, we assume a uniform mechanical frequency Ω_M, damping rate Γ_M, and coupling strength g_M. Owing to the optomechanical coupling at the first node, the oscillation condition can be expressed as

$$\Gamma_{\mathrm{OM}} > \Gamma_M + \Gamma_C,$$

where Γ_{OM} is the optomechancial gain and Γ_C is the rate of dissipation to the other coupled nodes. Here, we have taken into account the following coupled mode equations:

$$\begin{aligned}
&\ddot{x}_1 + \Gamma_M \dot{x}_1 + \Omega_M^2 x_1 + g_M \Omega_M x_2 = F_{\mathrm{OM}},\\
&\ddot{x}_2 + \Gamma_M \dot{x}_2 + \Omega_M^2 x_2 + g_M \Omega_M x_1 + g_M \Omega_M x_3 = 0,\\
&\vdots\\
&\ddot{x}_N + \Gamma_M \dot{x}_N + \Omega_M^2 x_N + g_M \Omega_M x_{N-1} = 0,
\end{aligned}$$

where x_i is the mechanical displacement of node i, and F_{OM} is the optomechanical force exerted on the first node. Note that we ignore the Langevin force. The mechanical displacements $(x_2, x_3, \ldots, x_N)$ are regarded as a dissipation channel (i.e., waveguide mode) by transforming to the waveguide basis $(w_2, w_3, \cdots, w_N)$ given by

$$w_k = \sqrt{\frac{2}{N}} \sum_{l=2}^{N} \sin\left(\frac{(k-1)(l-1)\pi}{N}\right) x_l,$$

where the factor of $\sqrt{2/N}$ is derived from the requirement for a unitary transformation (i.e., energy conservation). Importantly, the inverse transformation is equivalent; that is to say, replacement of w_i by x_i gives a similar form. Thus, by taking the Fourier transform, we can rewrite the coupled mode equations in the frequency domain,

$$\chi_M(\omega) x_1(\omega) + \frac{\sqrt{2} g_M \Omega_M}{\sqrt{N}} \sum_{l=2}^{N} \sin\left(\frac{l\pi}{N}\right) w_l(\omega) = F_{\mathrm{OM}}, \tag{C1}$$

$$\left[\chi_M(\omega) + 2 g_M \Omega_M \cos\left(\frac{(k-1)\pi}{N}\right)\right] w_k(\omega) + \frac{\sqrt{2} g_M \Omega_M}{\sqrt{N}} \sin\left(\frac{(k-1)\pi}{N}\right) x_1(\omega) = 0, \tag{C2}$$

where $\chi_M(\omega) \equiv (\Omega_M^2 - \omega^2) - i\omega\Gamma_M$ and the factor $2 g_M \Omega_M \cos\left((k-1)\pi/N\right)$ is derived as the eigenvalue of the corresponding waveguide mode. By substituting Eq. (C2) into Eq. (C1), the dynamics of x_1 becomes

$$\left[\chi_M(\omega) + \frac{2}{N} \sum_{l=1}^{N-1} \frac{g_M^2 \Omega_M^2}{\left(\chi(\omega) + 2 g_M \Omega_M \cos\left(\frac{l\pi}{N}\right)\right)} \times \sin\left(\frac{(l+1)\pi}{N}\right) \sin\left(\frac{l\pi}{N}\right) - F_{\mathrm{OM}}\right] x_1(\omega) = 0.$$

Thus, the oscillation condition is achieved by taking account of the imaginary part of the total susceptibility, i.e.,

$$\Gamma_M + \sum_{l=1}^{N-1} \Gamma_{C(l+1)} < \Gamma_{\mathrm{OM}}, \tag{C3}$$

where we have defined $\mathrm{Im}[F_{\mathrm{OM}}] = \omega\Gamma_{\mathrm{OM}}$ and $\Omega_l \equiv 2 g_M \cos(l\pi/N)$. The left-hand sides in Eq. (C3) can be further reduced to

$$\begin{aligned}
&\Gamma_M + \frac{g_M^2 \Omega_M^2}{N} \sum_{l=1}^{N-1} \frac{\Gamma_M}{(\omega^2 - \Omega_M^2 + \Omega_M \Omega_l)^2 + \omega^2 \Gamma_M^2} \times \left[1 - \cos\left(\frac{(2l+1)\pi}{N}\right)\right]\\
&\approx \Gamma_M + \frac{g_M^2}{\Gamma_M N} \sum_{l=1}^{N-1} \left[1 - \cos\left(\frac{(2l+1)\pi}{N}\right)\right]\\
&\approx \Gamma_M + \frac{g_M^2}{\Gamma_M},
\end{aligned}$$

where the first approximation uses $g_M \ll \Omega_M$ and $\omega \approx \Omega_M$, and the second one uses $\sum_{l=1}^{N-1}(1-\cos((2k+1)\pi/(N))) \approx N$ with $N \gg 1$. By defining $g_M = \eta\Gamma_M$, we can derive the condition for the local parametric oscillation as

$$\Gamma_M(1+\eta^2) < \Gamma_{\mathrm{OM}}. \tag{C4}$$

In a similar manner, we can determine the condition for the collective parametric oscillation, where a hybridized mechanical mode is collectively oscillating, by considering the hybridized mode in all the microbottles. This leads to the coupled mode equations

$$\chi'_M(\omega)h_l(\omega) = \sqrt{\frac{2}{N+1}}\sin\left(\frac{l\pi}{N+1}\right)F_{\mathrm{OM}},$$

where $h_l(\omega)$ is the hybridized displacement with $l = 1,\ldots,N$, and $\chi'_M(\omega)$ is the total susceptibility including the eigenvalue of the hybridized mode. Because the optomechanical gain is proportional to the square of the optomechanical coupling rate, it is renormalized to $\Gamma'_{\mathrm{OM},k} = 2/(N+1)\sin^2[k\pi/(N+1)]\,\Gamma_{\mathrm{OM}}$. Thus, the condition for the global oscillation regime is given by

$$\frac{N+1}{2}\Gamma_M < \Gamma_{\mathrm{OM}}, \tag{C5}$$

which oscillations preferably occur in the device is determined by comparing Eqs. (C4) and (C5). Thus, an oscillation factor defined as

$$\alpha_{\mathrm{osc}} = \frac{2(1+\eta_{\mathrm{min}}^2)}{N+1},$$

is used as an index for the parametric oscillation, where η_{min} is the minimum mechanical coupling factor among the multiple mechanical modes (RBMs). $\alpha_{\mathrm{osc}} < 1$ reflects that the CMBR causes the local parametric oscillation; $\alpha_{\mathrm{osc}} > 1$ reflects that it causes the collective parametric oscillation.

The coupling coefficient η_{ij} between the ith-order axial mode in the microbottle A and the j th-order axial mode in the microbottle B can be estimated by calculating the mode overlap integral,

$$\eta_{ij} = \frac{\sqrt{\Omega_A\Omega_B}}{\sqrt{\Gamma_A\Gamma_B}}\frac{\int \mathrm{d}V \boldsymbol{u}_A^{(i)}(r,z)\cdot\boldsymbol{u}_B^{(j)}(r,z)}{\sqrt{\int \mathrm{d}V|\boldsymbol{u}_A^{(i)}(r,z)|^2}\sqrt{\int \mathrm{d}V|\boldsymbol{u}_B^{(j)}(r,z)|^2}},$$

where $\boldsymbol{u}_k^{(i)}(r,z)$, Ω_k, and Γ_k are the spatial distribution of the ith-order axial mode, mechanical resonance frequency, and damping factor of microbottle k, respectively ($k = A, B$). By utilizing the analytical expression of the mechanical modes [19], the minimum coupling coefficient between the first-order axial modes is determined to be $\eta_{\mathrm{min}} = \eta_{11} = 0.5$. Thus, $\alpha_{\mathrm{osc}} = 0.05 < 1$ reflects that the local parametric oscillation preferably occurs in the CMBR.

For simplicity, the above discussion assumed that the optomechanical gain is independent of the mechanical modes. In practice, it depends on the mechanical frequencies through the laser detuning. For the second-order axial mode, $\eta_{22} = 7.8$, which is close to the experimental value of $\eta_{22}^{\mathrm{exp}} = 6.9$ estimated from coupled mode theory [19]. Because $\alpha_{\mathrm{osc}}^{\mathrm{2nd}} = 2.4 > 1$, a collective parametric oscillation can be achieved by finely adjusting the laser detuning to selectively provide optomechanical gain to the higher-order modes.

[1] M. Aspelmeyer, T. J. Kippenberg, and F. Marquardt, Cavity optomechanics, Rev. Mod. Phys. **86**, 1391 (2014).

[2] F. Massel, S. U. Cho, J.-M. Pirkkalainen, P. J. Hakonen, T. T. Heikkilä, and M. A. Sillanpää, Multimode circuit optomechanics near the quantum limit, Nat. Commun. **3**, 987 (2012).

[3] D. Lee, M. Underwood, D. Mason, A. Shkarin, S. Hoch, and J. Harris, Multimode optomechanical dynamics in a cavity with avoided crossings, Nat. Commun. **6**, 6232 (2015).

[4] F. Ruesink, M.-A. Miri, A. Alu, and E. Verhagen, Nonreciprocity and magnetic-free isolation based on optomechanical interactions, Nat. Commun. **7**, 13662 (2016).

[5] W. H. P. Nielsen, Y. Tsaturyan, C. B. Møller, E. S. Polzik, and A. Schliesser, Multimode optomechanical system in the quantum regime, Proc. Natl Acad. Sci. USA **114**, 62 (2017).

[6] H. Jing, S. Özdemir, X.-Y. Lü, J. Zhang, L. Yang, and F. Nori, *PT*-symmetric phonon laser, Phys. Rev. Lett. **113**, 053604 (2014).

[7] H. Xu, D. Mason, L. Jiang, and J. Harris, Topological energy transfer in an optomechanical system with exceptional points, Nature **537**, 80 (2016).

[8] J. Zhang, B. Peng, Ş. K. Özdemir, K. Pichler, D. O. Krimer, G. Zhao, F. Nori, Y.-X. Liu, S. Rotter, and L. Yang, A phonon laser operating at an exceptional point, Nat. Photonics **12**, 479 (2018).

[9] P. D. García, R. Bericat-Vadell, G. Arregui, D. Navarro-Urrios, M. Colombano, F. Alzina, and C. M. Sotomayor-Torres, Optomechanical coupling in the Anderson-localization regime, Phys. Rev. B **95**, 115129 (2017).

[10] G. Arregui, N. D. Lanzillotti-Kimura, C. M. Sotomayor-Torres, and P. D. García, Anderson photon-phonon colocalization in certain random superlattices, Phys. Rev. Lett. **122**, 043903 (2019).

[11] G. Arregui, R. C. Ng, M. Albrechtsen, S. Stobbe, C. Sotomayor-Torres, and P. D. García, Cavity optomechanics with Anderson-localized optical modes, Phys. Rev. Lett. **130**, 043802 (2023).

[12] K. Fang, J. Luo, A. Metelmann, M. H. Matheny, F. Marquardt, A. A. Clerk, and O. Painter, Generalized non-reciprocity in an optomechanical circuit via synthetic magnetism and reservoir engineering, Nat. Phys. **13**, 465 (2017).

[13] J. P. Mathew, J. d. Pino, and E. Verhagen, Synthetic gauge fields for phonon transport in a nano-optomechanical system, Nat. Nanotech. **15**, 198 (2020).

[14] H. Ren, T. Shah, H. Pfeifer, C. Brendel, V. Peano, F. Marquardt, and O. Painter, Topological phonon transport in an optomechanical system, Nat. Commun. **13**, 3476 (2022).

[15] J. J. Slim, C. C. Wanjura, M. Brunelli, J. del Pino, A. Nunnenkamp, and E. Verhagen, Optomechanical realization of the bosonic Kitaev-Majorana chain, arXiv:2309.05825 (2023).

[16] M. Zhang, S. Shah, J. Cardenas, and M. Lipson, Synchronization and phase noise reduction in micromechanical oscillator arrays coupled through light, Phys. Rev. Lett. **115**, 163902 (2015).

[17] M. Pöllinger, D. O'Shea, F. Warken, and A. Rauschenbeutel, Ultrahigh-Q tunable whispering-gallery-mode microresonator, Phys. Rev. Lett. **103**, 053901 (2009).

[18] Z.-H. Zhou, C.-L. Zou, Y. Chen, Z. Shen, G.-C. Guo, and C.-H. Dong, Broadband tuning of the optical and mechanical modes in hollow bottle-like microresonators, Opt. Express **25**, 4046 (2017).

[19] M. Asano, H. Yamaguchi, and H. Okamoto, Free-access optomechanical liquid probes using a twin-microbottle resonator, Sci. Adv. **8**, eabq2502 (2022).

[20] M. Asano, H. Yamaguchi, and H. Okamoto, Cavity optomechanical mass sensor in water with sub-femtogram resolution, Appl. Phys. Express **16**, 032002 (2023).

[21] A. MacDonald, B. Hauer, X. Rojas, P. Kim, G. Popowich, and J. Davis, Optomechanics and thermometry of cryogenic silica microresonators, Phys. Rev. A **93**, 013836 (2016).

[22] M. Asano, Y. Takeuchi, W. Chen, Ş. K. Özdemir, R. Ikuta, N. Imoto, L. Yang, and T. Yamamoto, Observation of optomechanical coupling in a microbottle resonator, Laser Photonics Rev. **10**, 603 (2016).

[23] S. Spillane, T. Kippenberg, O. Painter, and K. Vahala, Ideality in a fiber-taper-coupled microresonator system for application to cavity quantum electrodynamics, Phys. Rev. Lett. **91**, 043902 (2003).

[24] T. Carmon, L. Yang, and K. J. Vahala, Dynamical thermal behavior and thermal self-stability of microcavities, Opt. Express **12**, 4742 (2004).

[25] M. Gorodetksy, A. Schliesser, G. Anetsberger, S. Deleglise, and T. J. Kippenberg, Determination of the vacuum optomechanical coupling rate using frequency noise calibration, Opt. Express **18**, 23236 (2010).

[26] F. Liu, S. Alaie, Z. C. Leseman, and M. Hossein-Zadeh, Sub-pg mass sensing and measurement with an optomechanical oscillator, Opt. Express **21**, 19555 (2013).

[27] W. Yu, W. C. Jiang, Q. Lin, and T. Lu, Cavity optomechanical spring sensing of single molecules, Nat. Commun. **7**, 12311 (2016).

[28] B. Guha, P. E. Allain, A. Lemaitre, G. Leo, and I. Favero, Force sensing with an optomechanical self-oscillator, Phys. Rev. Appl. **14**, 024079 (2020).

[29] T. Kippenberg, H. Rokhsari, T. Carmon, A. Scherer, and K. Vahala, Analysis of radiation-pressure induced mechanical oscillation of an optical microcavity, Phys. Rev. Lett. **95**, 033901 (2005).

[30] M. Sumetsky and Y. Dulashko, Snap: Fabrication of long coupled microresonator chains with sub-angstrom precision, Opt. Express **20**, 27896 (2012).

[31] D. Hatanaka, I. Mahboob, K. Onomitsu, and H. Yamaguchi, Phonon waveguides for electromechanical circuits, Nat. Nanotech. **9**, 520 (2014).

[32] M. Xiao, G. Ma, Z. Yang, P. Sheng, Z. Zhang, and C. T. Chan, Geometric phase and band inversion in periodic acoustic systems, Nat. Phys. **11**, 240 (2015).

[33] I. Kim, S. Iwamoto, and Y. Arakawa, Topologically protected elastic waves in one-dimensional phononic crystals of continuous media, Appl. Phys. Express **11**, 017201 (2017).

[34] M. Esmann, F. R. Lamberti, P. Senellart, I. Favero, O. Krebs, L. Lanco, C. G. Carbonell, A. Lemaître, and N. D. Lanzillotti-Kimura, Topological nanophononic states by band inversion, Phys. Rev. B **97**, 155422 (2018).

[35] F. Monifi, J. Zhang, Ş. K. Özdemir, B. Peng, Y.-X. Liu, F. Bo, F. Nori, and L. Yang, Optomechanically induced stochastic resonance and chaos transfer between optical fields, Nat. Photonics **10**, 399 (2016).

[36] D. Navarro-Urrios, N. E. Capuj, M. F. Colombano, P. D. García, M. Sledzinska, F. Alzina, A. Griol, A. Martínez, and C. M. Sotomayor-Torres, Nonlinear dynamics and chaos in an optomechanical beam, Nat. Commun. **8**, 14965 (2017).

[37] R. Leijssen, G. R. La Gala, L. Freisem, J. T. Muhonen, and E. Verhagen, Nonlinear cavity optomechanics with nanomechanical thermal fluctuations, Nat. Commun. **8**, ncomms16024 (2017).

[38] J. Zhang, B. Peng, S. Kim, F. Monifi, X. Jiang, Y. Li, P. Yu, L. Liu, Y.-x. Liu, A. Alù, *et al.*, Optomechanical dissipative solitons, Nature **600**, 75 (2021).

[39] A. Seif, W. DeGottardi, K. Esfarjani, and M. Hafezi, Thermal management and non-reciprocal control of phonon flow via optomechanics, Nat. Commun. **9**, 1207 (2018).

[40] C. Yang, X. Wei, J. Sheng, and H. Wu, Phonon heat transport in cavity-mediated optomechanical nanoresonators, Nat. Commun. **11**, 4656 (2020).

[41] J.-Y. Liu, W. Liu, D. Xu, J.-C. Shi, H. Xu, Q. Gong, and Y.-F. Xiao, Ground-state cooling of multiple near-degenerate mechanical modes, Phys. Rev. A **105**, 053518 (2022).

[42] J. Huang, D.-G. Lai, C. Liu, J.-F. Huang, F. Nori, and J.-Q. Liao, Multimode optomechanical cooling via general dark-mode control, Phys. Rev. A **106**, 013526 (2022).

[43] G. Bahl, K. H. Kim, W. Lee, J. Liu, X. Fan, and T. Carmon, Brillouin cavity optomechanics with microfluidic devices, Nat. Commun. **4**, 1994 (2013).

[44] E. Gil-Santos, C. Baker, D. Nguyen, W. Hease, C. Gomez, A. Lemaître, S. Ducci, G. Leo, and I. Favero, High-frequency nano-optomechanical disk resonators in liquids, Nat. Nanotech. **10**, 810 (2015).

[45] E. Gil-Santos, J. J. Ruz, O. Malvar, I. Favero, A. Lemaître, P. M. Kosaka, S. García-López, M. Calleja, and J. Tamayo, Optomechanical detection of vibration modes of a single bacterium, Nat. Nanotech. **15**, 469 (2020).

[46] D. Navarro-Urrios, E. Kang, P. Xiao, M. F. Colombano, G. Arregui, B. Graczykowski, N. E. Capuj, M. Sledzinska, C. M. Sotomayor-Torres, and G. Fytas, Optomechanical

crystals for spatial sensing of submicron sized particles, Sci. Rep. **11**, 7829 (2021).

[47] P. W. Anderson, Absence of diffusion in certain random lattices, Phys. Rev. **109**, 1492 (1958).

[48] M. Spletzer, A. Raman, H. Sumali, and J. P. Sullivan, Highly sensitive mass detection and identification using vibration localization in coupled microcantilever arrays, Appl. Phys. Lett. **92**, 114102 (2008).